LETTERS
https://doi.org/10.1038/s41563-020-00865-5

nature materials

Check for updates

Visualization of dynamic polaronic strain fields in hybrid lead halide perovskites

Burak Guzelturk[1,2,3], Thomas Winkler[4,5], Tim W. J. Van de Goor[4], Matthew D. Smith[6], Sean A. Bourelle[4], Sascha Feldmann[4], Mariano Trigo[1], Samuel W. Teitelbaum[1], Hans-Georg Steinrück[7,8], Gilberto A. de la Pena[1], Roberto Alonso-Mori[9], Diling Zhu[9], Takahiro Sato[9], Hemamala I. Karunadasa[1,6], Michael F. Toney[7], Felix Deschler[4,10] and Aaron M. Lindenberg[1,2,11] ✉

Excitation localization involving dynamic nanoscale distortions is a central aspect of photocatalysis[1], quantum materials[2] and molecular optoelectronics[3]. Experimental characterization of such distortions requires techniques sensitive to the formation of point-defect-like local structural rearrangements in real time. Here, we visualize excitation-induced strain fields in a prototypical member of the lead halide perovskites[4] via femtosecond resolution diffuse X-ray scattering measurements. This enables momentum-resolved phonon spectroscopy of the locally distorted structure and reveals radially expanding nanometre-scale strain fields associated with the formation and relaxation of polarons in photoexcited perovskites. Quantitative estimates of the magnitude and shape of this polaronic distortion are obtained, providing direct insights into the dynamic structural distortions that occur in these materials[5–9]. Optical pump–probe reflection spectroscopy corroborates these results and shows how these large polaronic distortions transiently modify the carrier effective mass, providing a unified picture of the coupled structural and electronic dynamics that underlie the optoelectronic functionality of the hybrid perovskites.

In the past decade the lead halide perovskite material system has shown exceptional promise in optoelectronics due to its long carrier lifetimes and carrier diffusion lengths, high photoluminescence quantum yields and defect tolerance[4]. These properties prevail in a material that is grown inexpensively by low temperature solution-processing techniques, and have attracted intensive efforts to understand their microscopic mechanisms. Different hypotheses have been proposed, which involve the crucial role of dynamic local distortions, including polaron formation[5–7], dynamic Rashba effects[10] and local ferroelectric fluctuations[11]. Although prior work has established the important contributions of dynamic structural responses, the proposed lattice–carrier coupling mechanisms have not been fully understood and the geometry and dynamics of these distortions have not been precisely estimated, in part due to the challenge of tracking atomic-scale motions which form transiently following photon absorption[12].

In recent work, the formation of large polarons in hybrid perovskites has been inferred indirectly from terahertz spectroscopy or other optical approaches, showing strong electron–longitudinal optical phonon coupling[9,13,14]. Reports have also highlighted anomalies in the far-infrared dielectric function, suggesting complex carrier–lattice interactions in the form of ferroelectric polarons[15], solvated polarons[16] or hyperpolarons[17]. These imply collective lattice deformations occurring after photoexcitation, yet the nature of the polaron, the associated elastic strain field and its spatio-temporal evolution remain unclear. To measure these distortions, in this Letter we use femtosecond X-ray pulses to perform optical pump X-ray diffuse scattering probe measurements on single crystal methylammonium lead bromide ($(MA)PbBr_3$), carried out at the Linac Coherent Light Source (LCLS)[18]. This involves the time-domain application of longstanding approaches for studying lattice relaxation around point defects via measurements of the diffuse tails of Bragg peaks[19] and enables a reconstruction of the transient elastic strain field associated with polaronic lattice distortions.

Figure 1a shows the experimental scattering geometry (further details in Methods and Supplementary Sections 1 and 2). The high X-ray energy (13.5 keV) enabled probing of multiple Bragg peaks simultaneously. To vary the X-ray incidence angle with respect to the crystal plane, the crystal is rotated azimuthally about its surface normal (ϕ) (Fig. 1b). We first discuss the results with respect to the (−1 −3 2) reflection. With X-rays incident along the [100] direction, the (−1 −3 2) set of lattice planes approximately satisfies the Bragg condition. A rotation by $\Delta\phi$ about the surface normal rotates the corresponding reciprocal lattice vector and leads to a continuous change in the X-ray incidence angle $\Delta\theta$ with respect to the Bragg angle (θ_B) thus mapping out a rocking curve (see Supplementary Section 3). A deviation in incidence and scattering angle $\Delta\theta$ leads to a momentum mismatch, which is compensated by scattering inelastically off a phonon of wave vector $\mathbf{q}$. The probed wave vector $\mathbf{q}$ is related to $\Delta\theta$ by $q = G\cot\theta_B\Delta\theta$, where G is the reciprocal lattice vector[20,21] (see Fig. 1b). Figure 1c shows the transient diffracted signal intensity ($\Delta I/I_0$) after 400 nm above-gap excitation measured at two different $\Delta\phi$ values corresponding to (1) near the Bragg condition ($q \approx 0$) and (2) away from the Bragg condition ($q = 0.4\,nm^{-1}$). While the response for $q = 0.4\,nm^{-1}$ is prompt and starts at time zero, the response for $q \approx 0$ is anomalously delayed by ~20 ps. Probing

[1]Stanford Institute for Materials and Energy Sciences, SLAC National Accelerator Laboratory, Menlo Park, CA, USA. [2]Department of Materials Science and Engineering, Stanford University, Stanford, CA, USA. [3]X-ray Science Division, Advanced Photon Source, Argonne National Laboratory, Lemont, IL, USA. [4]Cavendish Laboratory, University of Cambridge, Cambridge, UK. [5]Department of Physics and Astronomy, Aarhus University, Aarhus C, Denmark. [6]Department of Chemistry, Stanford University, Stanford, CA, USA. [7]Stanford Synchrotron Radiation Laboratory Lightsource, SLAC National Accelerator Laboratory, Menlo Park, CA, USA. [8]Department of Chemistry, Paderborn University, Paderborn, Germany. [9]Linac Coherent Light Source, SLAC National Accelerator Laboratory, Menlo Park, CA, USA. [10]Walter Schottky Institute, Department of Physics, Technical University of Munich, Garching, Germany. [11]PULSE Institute, SLAC National Accelerator Laboratory, Menlo Park, CA, USA. ✉e-mail: aaronl@stanford.edu

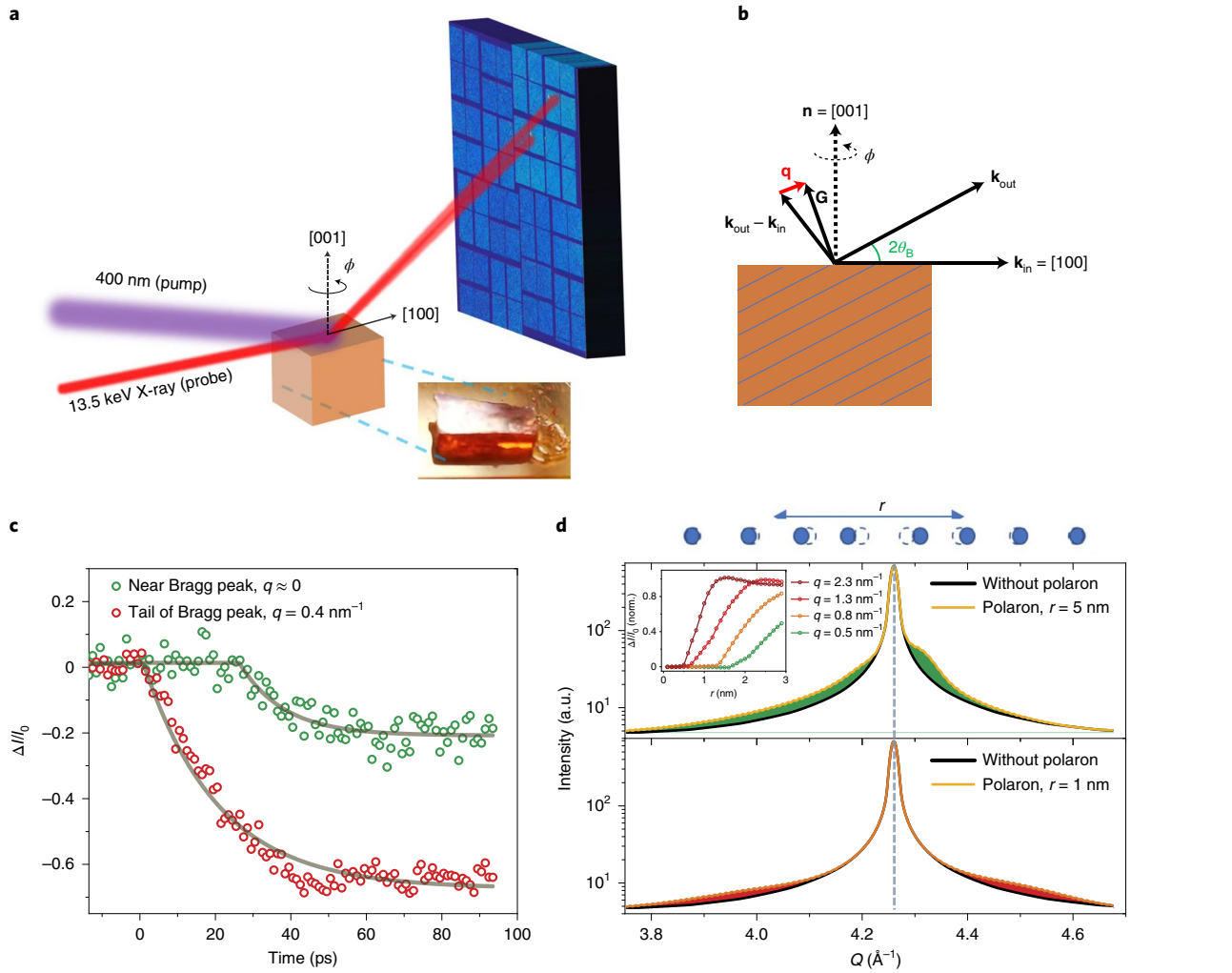

Fig. 1 | Experimental setup and observation of temporally delayed transient structural responses. a, Experimental setup showing diffraction geometry and associated crystallographic directions of the cubic (MA)$PbBr_3$ single crystal. Monochromatized femtosecond X-ray pulses (13.5 keV) were incident on (MA)$PbBr_3$ at a grazing angle of 0.3°, matching the X-ray penetration depth with that of above-gap 400 nm femtosecond optical pulses. Diffracted X-rays from lattice planes non-parallel to the crystal surface were recorded on a large area detector and read out on a shot-by-shot basis. The inset shows a photo of the (MA)$PbBr_3$ single crystal used for the experiment. **b**, Schematic showing wave vector matching diagram defining probed phonon wave vector **q** as a function of rotation ϕ about the crystal normal (**n** = [001]). The X-rays were incident along $\mathbf{k}_{in}$ = [100]. **G** is the reciprocal lattice vector. θ_B is the Bragg angle and $\mathbf{k}_{out}$ is the scattered X-ray vector. **c**, Transient scattering intensity of (−1 −3 2) reflection measured near the Bragg peak (green) ($q \approx 0$) and in the tail region (red) ($q = 0.4\,nm^{-1}$), corresponding to different probed phonon wave vectors. The structural response is prompt, starting at time zero for $q = 0.4\,nm^{-1}$, but is delayed by tens of picoseconds as q approaches 0. Lines are a guide to the eye. **d**, One-dimensional rocking curve model showing impact of polaronic distortions of radius $r = 1$ nm (bottom) and 5 nm (top) in comparison with the no-distortion case. Shaded regions show the induced diffuse signals in the rocking curve due to the polaronic distortions. Inset shows diffracted intensity for various q values near the Bragg peak, showing q-dependent non-linear responses as a function of polaron radius, which acts like a proxy for the delay time in the experiment.

responses at wave vector **q** enables measurement of the associated distortions in real-space with a length scale $\approx 1/q$. Thus, Fig. 1c indicates spatio-temporal evolution of the local lattice distortions after excitation.

To provide a first-order understanding of this delayed response, we simulate rocking curves by calculating the Fourier transform of a one-dimensional chain of atoms with a Gaussian distortion of variable radius r starting at the centre (Supplementary Section 4). Figure 1d shows the simulated rocking curves for two different distortions, with $r = 1$ nm and $r = 5$ nm compared to the undistorted case. In this model, nanoscale strain fields give rise to changes in the tails of the Bragg peak (often referred to as Huang scattering[22]). The distortion-induced signal in the diffuse region moves in towards the Bragg peak (to lower q) as the distortion expands in real-space giving rise to a threshold-like response depending on the radius (Fig. 1d inset). Thus, the size of the local distortion acts as a proxy for the onset delay time, and the difference in delay times probed at different q indicates the growth kinetics of the photo-induced local distortions over picosecond timescales and nanometre length scales. Figure 2a–c summarizes the full q-dependent response for the (−1 −3 2) Bragg peak at a pump fluence of 280 μJ cm^{-2}. A continuous variation in the measured delays is observed as a function of q (Fig. 2b,c). Signals probed for large q exhibit prompt responses while responses become progressively more delayed as $q = 0$ is approached. The magnitude of $\Delta I/I_0$ is also asymmetric with q and changes sign on opposite sides of the Bragg peak. We show in Supplementary Section 5 that the sign of the asymmetry is indicative of an expansive strain field, consistent across all measured

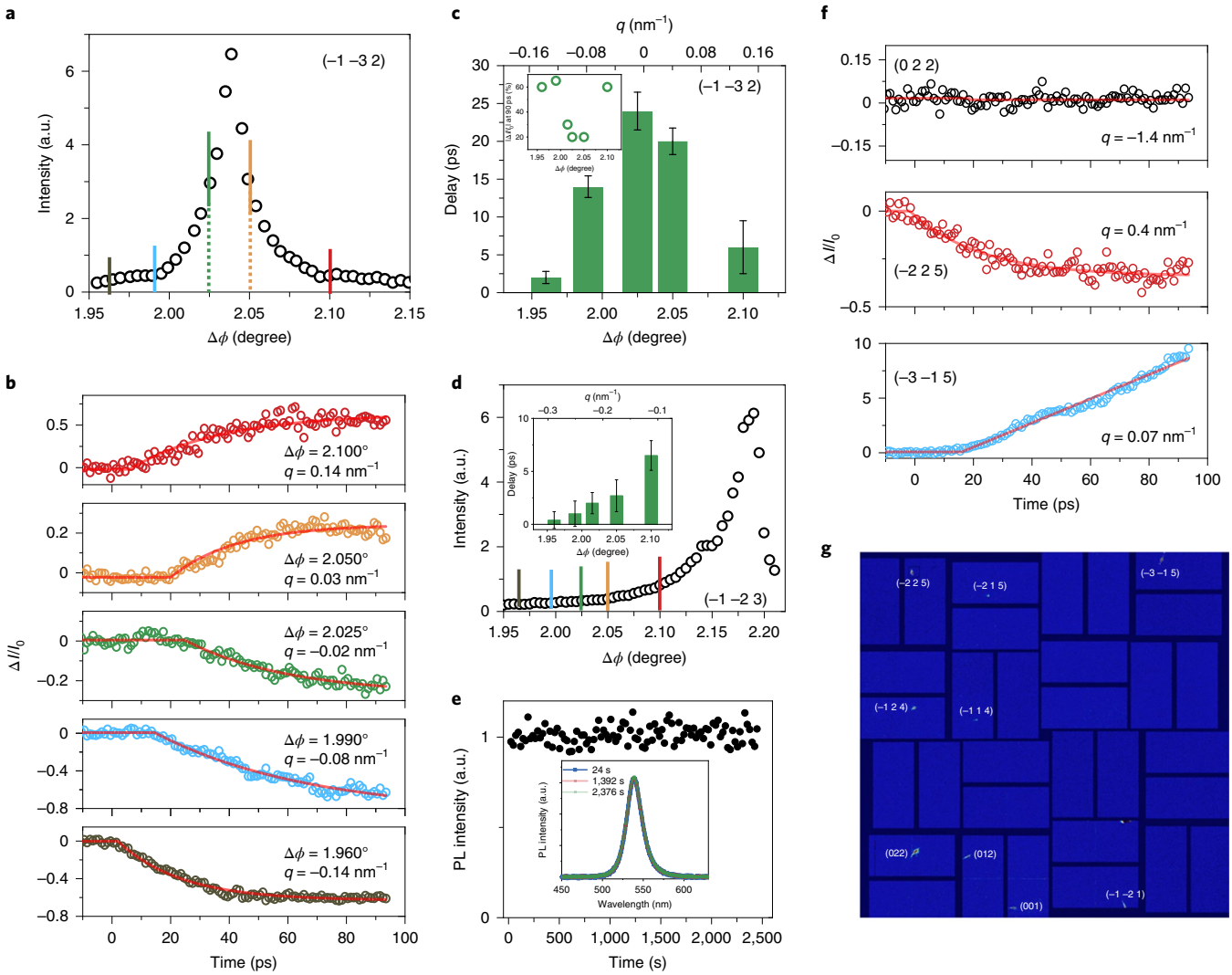

Fig. 2 | Phonon-momentum-resolved time scans for selected Bragg peaks. a, Sampled rocking curve for the (−1 −3 2) reflection as a function of rotation of the crystal about its normal ($\Delta\phi$). **b**, Time-resolved intensity changes for various colour-coded positions with respect to the Bragg peak shown in **a**. **c**, Measured onset delay with respect to the time zero as a function of deviation from the Bragg peak in $\Delta\phi$ and q. Error bars show the standard error. Inset shows the magnitude of the relative intensity change at 90 ps as a function of q. **d**, Sampled rocking curve for the (−1 −2 3) reflection. Time-resolved intensity changes for various colour-coded positions with respect to the Bragg peak are shown in Supplementary Section 6. Inset shows the measured onset delay with respect to time zero as a function of deviation from the Bragg peak in $\Delta\phi$ and q. Error bars show the standard error. **e**, Photoluminescence (PL) intensity over time. Inset shows the spectrum of the photoluminescence at 24, 1,392 and 2,376 s. **f**, Time-resolved response for other measured Bragg peaks comparing (top) large q where the effects are damped out, (middle) intermediate q where the effects grow quickly with time, and (bottom) near-zero q where the response is substantially delayed. **g**, Diffraction image showing multiple Bragg peaks measured simultaneously.

Bragg peaks. These observations hold for the full range of probed fluences between 20 and 280 μJ cm^{-2} (Supplementary Section 7). Figure 2e shows no change in photoluminescence of the sample over a 40-minute exposure time, indicating that the sample stability was preserved.

Measurements on other Bragg peaks provide a self-consistent picture with the discussion above. For the probed $\Delta\phi$ values in Fig. 2c, we simultaneously probed the tail region of the (−1 −2 3) reflection (Fig. 2d). In this case, q varies from −0.3 to −0.1 nm^{-1} and the onset delays become progressively elongated (Supplementary Section 6). Probing $q \approx 0$ in this peak also shows a 25 ps delay (see Supplementary Fig. 6) consistent with that of the (−1 −3 2) reflection. Figure 2f shows time scans probing the (0 2 2), (−2 2 5) and (−3 −1 5) reflections corresponding to large (q = −1.4 nm^{-1}), intermediate (q = 0.4 nm^{-1}) and small (q = 0.07 nm^{-1}) configurations, respectively. While the signal magnitude is negligible for large q, as shown for the (0 2 2) reflection, effects with opposite sign are observed for the (−2 2 5) and (−3 −1 5) reflections. These responses are all consistent with expansive-type strains (Supplementary Section 5). In all cases, the magnitude of the response starts small near q = 0, becomes larger in amplitude as the deviation is probed further into the tails, and then decreases at very high q (on both sides of the peak), such that there is a maximum in the effect size occurring at a non-zero q.

We now consider a model, motivated by prior studies of strain relaxation around point defects[19] and the one-dimensional calculation described above that allows the dynamically expanding shape of the polaronic strain field to be visualized. In particular, following calculations of the static diffuse scattering associated with dilute nanoscale elastic fields in three dimensions and in the limit of small

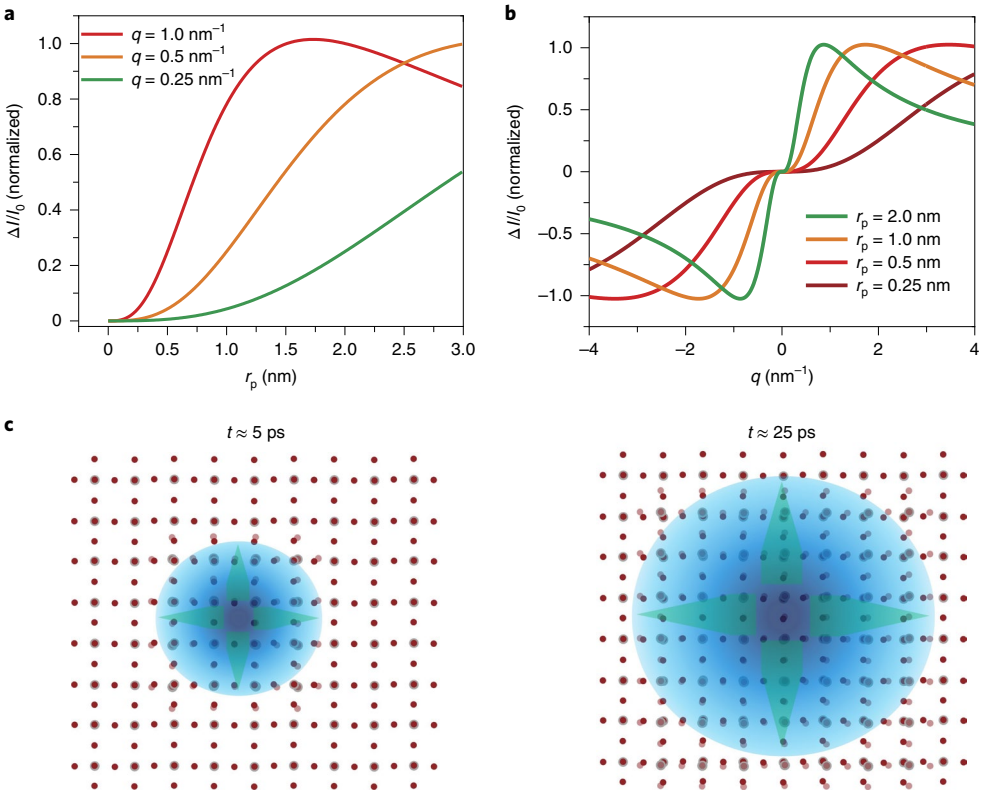

Fig. 3 | Analytical model for diffuse scattering from expanding polaronic strains. a, Calculated transient diffracted intensity change estimated for various q near the Bragg peak from equation (1), showing q-dependent responses as a function of polaron radius (r_p). For decreasing q, the transient signal emerges only for distortions larger than a threshold radius. **b**, Transient diffracted intensity change versus q estimated for polaronic distortions with different radii ranging from 0.25 to 2 nm. **c**, Schematic of the three-dimensional polaron model indicating the temporal evolution of the localized distortions in the perovskite lattice. Brown and grey colours represent bromide and lead atoms within the perovskite crystal structure, respectively. Blue shaded region and green arrows indicate the expansive strain associated with the developing polaronic distortions.

atomic displacements[22], we show in Supplementary Section 8, where variables are described in detail, that a radially symmetric elastic displacement field with a radius $r_p(t)$ given by $\boldsymbol{u}(\boldsymbol{r}) = u_r\hat{\boldsymbol{r}} = Ae^{-r/r_p(t)}\hat{\boldsymbol{r}}$ where A is the displacement amplitude, gives rise to a normalized modulation in the tails of the Bragg peaks given by

$$\left(\frac{\Delta I}{I}\right) = \frac{16}{3^{3/2}}\frac{q^3 r_p^3(t)}{\left(1+q^2 r_p^2(t)\right)^2} \qquad (1)$$

Equation (1) shows analytically the origin of the anomalous delayed onset responses, which grow non-linearly as $q^3 r_p^3$, giving rise to a q-dependent change in scattering intensity as a function of polaron radius ($r_p(t)$). At small q, probing features on long length scales, the elastic strain field needs to reach a large size to give rise to an observable effect (Fig. 3a). By contrast, at intermediate and high q, corresponding to short length scales, the response is prompt, near time zero, and is associated with a high sensitivity to short-range distortions. Figure 3b shows the estimated $\Delta I/I_0$ as a function of q for various r_p showing the asymmetry in the response, where the sign of the response flips. In equation (1), $\Delta I/I_0$ peaks as a function of r_p at $r_{p,max} = \frac{\sqrt{3}}{q}$ and as a function of q at $q_{max} = \frac{\sqrt{3}}{r_p}$, corresponding to an intermediate q for a polaron with a spatial extent of a few nanometres. Thus, a dynamically expanding polaronic strain field in response to the excitation of free carriers represents a self-consistent model, which quantitatively explains the full range of observed results, including (1) delayed onsets in the transient scattering intensity as a function of q, (2) transient responses starting at high q and sweeping inwards towards lower q, (3) an asymmetry in magnitude as a function of q, and (4) a signal which approaches zero at high and low q, thus reaching a maximum at some intermediate value. Qualitatively similar results are also obtained for other assumed spatial profiles besides the exponential fall-off assumed above (Supplementary Section 8). The similarity in the observed responses for different Bragg peaks implies a quasi-spherical expanding distortion (Fig. 3c) without a strong dependence on crystallographic direction. By comparing this model with the data in Fig. 2, we estimate a polaron radius of ~3 nm at $t = 20$ ps, spanning approximately ten unit cells. From this perspective, at long times this corresponds to a large polaron, consistent with prior hypotheses.[5,6] It is possible to estimate the magnitude of the distortions. For a fractional change on the order of one, as observed near q_{max} (Fig. 2), we show in Supplementary Section 8 that this requires $AGr_p^3/V \approx 1$ where V is the unit cell volume. For $r_p \approx 3$ nm, this gives an average strain $A/d \approx 0.1\%$, representing a notable distortion. The strain energy associated with a spherical phonon distortion of volume V_p is given by $1/2 V_p E(A/d)^2$ where E is Young's modulus (neglecting the contribution from optical phonon modes, discussed in Supplementary Section 10). The resultant energy of ~7 meV for the values above is in good agreement with the polaron binding energy estimated as $e^2/(4\pi\varepsilon_o\varepsilon r_p) \approx 10$ meV, with e the electron charge and $\varepsilon \approx 30$ the static dielectric constant[23], and with other theoretical estimates[5]. At longer times, after formation of the polaronic strain field, we observe a relaxation on timescales of hundreds of picoseconds to nanoseconds (Supplementary Section 9). This relaxation time is consistent with prior measurements of the photoluminescence lifetime at similar excitation fluences and further supports the carrier-induced origin of the strain. We note that these measurements are not capable of distinguishing the role of electrons versus holes on polarons.

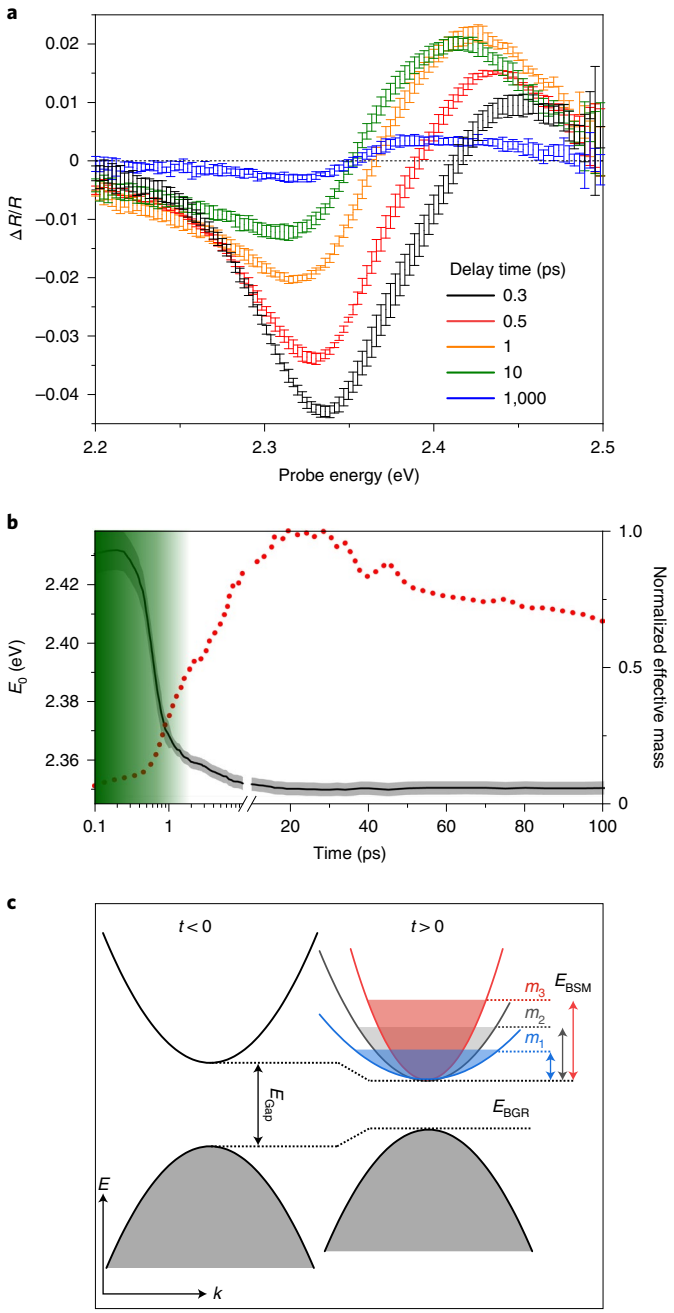

Fig. 4 | Ultrafast transient reflectivity studies and effects of polaron formation on optoelectronic properties. a, Transient reflection spectra taken at five different pump–probe time delays after excitation with a 400 nm pump pulse using a fluence of 20 μJ cm^{-2} (see other fluences in Supplementary Fig. 14). The horizontal dashed line indicates a transient change in reflectivity ($\Delta R/R$) of 0. The error bars represent the standard deviation of several ($\Delta R/R$) spectra taken at the respective time delays. **b**, $\Delta R/R$ zero-crossing (black line) with standard deviation (shaded area) and the corresponding calculated relative change in the normalized effective mass (red dotted line) as a function of pump–probe delay. The green shaded area indicates the timeframe in which E_0 and the effective mass are affected by carrier thermalization. **c**, Sketch of the dependence of bandgap renormalization 'BGR' and Burstein-Moss/band filling 'BSM' on the effective band gap energy. The different conduction band slopes on the right-side correlate to different effective electron masses, where m_3 (red) < m_2 (grey) < m_1 (blue) while the overall carrier density is the same.

To correlate the structural rearrangements discussed above with changes in the optoelectronic properties, we performed spectrally resolved transient reflection measurements under similar excitation conditions. We show that polaron formation can be linked to a time-dependent change in the effective mass of a carrier. Figure 4a shows the relative change in reflectivity for a range of selected time delays. Shortly after excitation, we observe a differential feature with a zero-crossing at 2.4 eV (black line), approximately 200 meV above the absorption onset measured by steady-state absorption (see Supplementary Section 11). The magnitude of the transient reflection signal decreases with increasing pump–probe delay time (Supplementary Fig. 13), due to radiative and non-radiative recombination. Importantly, the zero-crossing energy E_0 shifts by nearly 80 meV towards smaller energies within the first 20 ps (Fig. 4b, black line), which is notably longer than the intraband-thermalization timescale in (MA)$PbBr_3$ of a few picoseconds (Supplementary Section 11). While the initial red shift of E_0 on the 0–1 ps timescale can be linked to intraband-thermalization and band filling (indicated by the green shaded area), the subsequent shift can be correlated with changes in the optical band gap energy[24–26]. Additional measurements using quasi-resonant excitation at 505 nm presented in Supplementary Section 11 (Supplementary Fig. 17) further support this conclusion.

While many-body interactions of the excited carriers are known to reduce the band gap energy through band gap renormalization (BGR), the Burstein–Moss effect (BSM) (that is, band filling) will counter this effect (Fig. 4c)[27,28]. In addition to their expected dependence on the carrier density, the effective mass m^* of the carriers has a strong impact on these competing processes. Changes in the effective mass are expected to occur from the evolution of a polaronic strain field[29,30]. To confirm that the observed changes in E_0 can be caused by a relative change in the effective mass, we model the band-gap shifts that arise from band filling and band-gap renormalization, taking into account the dynamics of the overall carrier density after carrier thermalization. We extract the change in effective mass relative to its value determined from E_0 measured at a large time delay of 1.7 ns. This change in mass could arise from either carrier type (electron or hole), which cannot be distinguished by this approach. Figure 4b shows that the effective mass increases after excitation and reaches a maximum after ~20 ps. While the initial response on the 0–1 ps timescale is linked to intraband thermalization, we associate the continuous increase in the effective mass up to 20 ps with polaron formation, initially involving short-range distortions. Subsequently, the effective mass begins to decrease on a timescale of hundreds of picoseconds. This observation corroborates the observed growth of the strain fields towards larger length scales associated with carrier delocalization. This qualitative behaviour of the transient effective mass change is consistent over a range of excitation fluences spanning an order of magnitude (Supplementary Fig. 14), as with the X-ray data.

In summary, our results indicate that charge carriers in lead halide perovskites cause nanoscale structural distortions developing on picosecond timescales. Femtosecond resolution diffuse-scattering measurements resolve the time-dependent structure and enable quantitative measurements of the magnitude of local strain fields and their shape. The correlation between structural characterization and optical measurements provides a picture of the coupled structural and optoelectronic properties of charge carriers. The approach described here is general in its applicability and may be applied to a broad range of other materials in which dynamic structural heterogeneous responses underlie their functionality.

Online content

Any methods, additional references, Nature Research reporting summaries, source data, extended data, supplementary information, acknowledgements, peer review information; details of

author contributions and competing interests; and statements of data and code availability are available at https://doi.org/10.1038/s41563-020-00865-5.

Received: 21 May 2020; Accepted: 26 October 2020;
Published online: 4 January 2021

References

1. Carneiro, L. M. et al. Excitation-wavelength-dependent small polaron trapping of photoexcited carriers in α-Fe_2O_3. *Nat. Mater.* **16**, 819–825 (2017).
2. Koepsell, J. et al. Imaging magnetic polarons in the doped Fermi–Hubbard model. *Nature* **572**, 358–362 (2019).
3. Fratini, S., Ciuchi, S., Mayou, D., Trambly de Laissardière, G. & Troisi, A. A map of high-mobility molecular semiconductors. *Nat. Mater.* **16**, 998–1002 (2017).
4. Brenner, T. M., Egger, D. A., Kronik, L., Hodes, G. & Cahen, D. Hybrid organic–inorganic perovskites: low-cost semiconductors with intriguing charge-transport properties. *Nat. Rev. Mater.* **1**, 15007 (2016).
5. Zheng, F. & Wang, L.-w Large polaron formation and its effect on electron transport in hybrid perovskites. *Energy Environ. Sci.* **12**, 1219–1230 (2019).
6. Miyata, K. et al. Large polarons in lead halide perovskites. *Sci. Adv.* **3**, e1701217 (2017).
7. Ghosh, D., Welch, E., Neukirch, A. J., Zakhidov, A. & Tretiak, S. Polarons in halide perovskites: a perspective. *J. Phys. Chem. Lett.* **11**, 3271–3286 (2020).
8. Lan, Y. et al. Ultrafast correlated charge and lattice motion in a hybrid metal halide perovskite. *Sci. Adv.* **5**, eaaw5558 (2019).
9. Guzelturk, B. et al. Terahertz emission from hybrid perovskites driven by ultrafast charge separation and strong electron–phonon coupling. *Adv. Mater.* **30**, 1704737 (2018).
10. Stranks, S. D. & Plochocka, P. The influence of the Rashba effect. *Nat. Mater.* **17**, 381–382 (2018).
11. Frost, J. M. et al. Atomistic origins of high-performance in hybrid halide perovskite solar cells. *Nano Lett.* **14**, 2584–2590 (2014).
12. Wu, X. et al. Light-induced picosecond rotational disordering of the inorganic sublattice in hybrid perovskites. *Sci. Adv.* **3**, e1602388 (2017).
13. Cinquanta, E. et al. Ultrafast THz probe of photoinduced polarons in lead-halide perovskites. *Phys. Rev. Lett.* **122**, 166601 (2019).
14. Thouin, F. et al. Phonon coherences reveal the polaronic character of excitons in two-dimensional lead halide perovskites. *Nat. Mater.* **18**, 349–356 (2019).
15. Miyata, K. & Zhu, X.-Y. Ferroelectric large polarons. *Nat. Mater.* **17**, 379–381 (2018).
16. Guo, Y. et al. Dynamic emission Stokes shift and liquid-like dielectric solvation of band edge carriers in lead-halide perovskites. *Nat. Commun.* **10**, 1175 (2019).
17. Anusca, I. et al. Dielectric response: answer to many questions in the methylammonium lead halide solar cell absorbers. *Adv. Energy Mater.* **7**, 1700600 (2017).
18. Chollet, M. et al. The X-ray pump–probe instrument at the Linac Coherent Light Source. *J. Synchrotron Rad.* **22**, 503–507 (2015).
19. Peisl, H. Defect properties from X-ray scattering experiments. *J. Phys. Colloq.* **37**, C7–C47 (1976).
20. Lindenberg, A. M. et al. Time-resolved X-ray diffraction from coherent phonons during a laser-induced phase transition. *Phys. Rev. Lett.* **84**, 111–114 (2000).
21. Larsson, J. et al. Picosecond X-ray diffraction studies of laser-excited acoustic phonons in InSb. *Appl. Phys. A* **75**, 467–478 (2002).
22. Fultz, B. & Howe, J. M. *Transmission Electron Microscopy and Diffractometry of Materials* (Springer-Verlag, 2013).
23. Sendner, M. et al. Optical phonons in methylammonium lead halide perovskites and implications for charge transport. *Mater. Horiz.* **3**, 613–620 (2016).
24. Jani, H. & Duan, L. Time-frequency spectroscopy of GaAs transient dispersion using few-cycle pump-probe reflectometry. *Phys. Rev. Appl.* **13**, 054010 (2020).
25. Shcherbakov, M. R. et al. Ultrafast all-optical tuning of direct-gap semiconductor metasurfaces. *Nat. Commun.* **8**, 17 (2017).
26. Bennett, B. R., Soref, R. A. & Del Alamo, J. A. Carrier-induced change in refractive index of InP, GaAs and InGaAsP. *IEEE J. Quantum Electron.* **26**, 113–122 (1990).
27. Walsh, A., Da Silva, J. L. F. & Wei, S.-H. Origins of band-gap renormalization in degenerately doped semiconductors. *Phys. Rev. B* **78**, 075211 (2008).
28. Berggren, K. F. & Sernelius, B. E. Band-gap narrowing in heavily doped many-valley semiconductors. *Phys. Rev. B* **24**, 1971–1986 (1981).
29. Smart, T. J., Pham, T. A., Ping, Y. & Ogitsu, T. Optical absorption induced by small polaron formation in transition metal oxides: the case of Co_3O_4. *Phys. Rev. Mater.* **3**, 102401 (2019).
30. van Mechelen, J. L. M. et al. Electron-phonon interaction and charge carrier mass enhancement in $SrTiO_3$. *Phys. Rev. Lett.* **100**, 226403 (2008).

Methods

Optical pump/X-ray probe experiment. Monochromatized X-ray probe pulses of 13.5 keV energy were used, generated from the third harmonic of the fundamental at 4.5 keV, at the LCLS. The repetition rate of the X-rays was 120 Hz with a pulse duration of ~80 fs. The flux of the X-rays was kept low (~10^6 photons per pulse) to avoid any X-ray-induced damage to the perovskite sample. As reported in Fig. 2e, we used the photoluminescence intensity of the sample as a proxy for the sample stability. We observed that the sample was extremely stable over typical 40 min data acquisitions while the X-rays and optical pump beam were simultaneously incident on the sample. The X-rays were incident on the sample at a grazing incidence angle of 0.3° with the sample lying in the horizontal plane. The X-ray spot size at the sample location was 30 × 30 µm. Considering the incidence angle, the actual footprint of the probe on the sample was 30 µm × 5.7 mm.

Optical pump pulses at 400 nm were obtained by frequency doubling femtosecond pulses at 800 nm generated by a Ti:Sapphire laser. The pulse width of the pump was nominally 45 fs with a repetition rate of 120 Hz matched to the X-rays. Two cylindrical lenses were used to focus the beam on the sample surface, giving a spot size of 400 × 1400 µm at the sample location. The optical pump was incident on the sample at a grazing angle of 6°, almost collinear with the X-rays to minimize temporal walk-off. Thus, the footprint of the optical pump on the sample was 400 µm × 13.39 mm, overfilling the X-ray probe area. We did not observe any damage to the sample for excitation fluences below 1 mJ cm^{-2}. The polarization of the linearly polarized pump pulse was in the vertical plane to minimize reflection losses.

To estimate the penetration depth of the X-rays, we used the Center for X-ray Optics database for $(MA)PbBr_3$ composition (see Supplementary Fig. 1), which gives a penetration depth of 90 nm for the X-rays in the sample. This represents an upper bound with the actual X-ray probe depth being smaller since the scattered X-rays must exit the sample as well. Using the known optical absorption coefficient at 400 nm in the sample (1×10^5 cm^{-1}) this leads to an optical penetration depth of about 100 nm that matches well with that of the X-rays. For the X-ray detector, we used the standard large area CSPAD (Cornell-SLAC Pixel Array Detector) at the X-ray pump–probe (XPP) hutch at the LCLS, with diffraction patterns read out on a shot-by-shot basis.

Synthesis of $(MA)PbBr_3$ single crystal. The solvent *N*,*N*-dimethylformamide was dried and degassed using a solvent purification system (JC Meyer). In a 20 ml glass vial, $PbBr_2$ (1.1016 g) and (MA)Br (0.3427 g) were dissolved in *N*,*N*-dimethylformamide (16.0 ml) and sonicated to form a colourless solution. This solution stood for 10 min, and was then filtered through a 0.22 um polytetrafluoroethylene syringe filter to remove any remaining particulate matter. This solution was divided into eight portions (2 ml each), and each portion was used for vapour diffusion crystallization, with dimethoxyethane as the outer solvent. Crystals were isolated from the mother liquor by placing them in oil (paratone-N) and then washing three times with portions of hexanes to remove the oil.

Transient reflectivity measurements. Transient pump–probe reflection measurements were carried out using linearly polarized 800 nm 90 fs laser pulses, provided by a Ti:Sapphire amplifier system (Spectra Physics Solstice) operating at 1 kHz. The pump beam was frequency doubled in a beta barium borate crystal used to excite the sample. The pump repetition rate was reduced to 500 Hz using a motorized chopper wheel. In the probe path, the 800 nm pulse was frequency converted using a home-built non-collinear optical parametric amplifier into a spectrally broad probe pulse in the visible spectral region (500–620 nm). After the probe pulse was focused onto the sample and overlapped with the pump pulse, it was collected and sent into a grating spectrometer with spectral information recorded using a charge-coupled device camera.

Data availability

The data represented in Figs. 1, 2, 3 and 4 are provided with the paper as source data. Other datasets generated and/or analysed during the current study are available from A.M.L. upon reasonable request. Source data are provided with this paper.

Acknowledgements

This work is supported by the US Department of Energy (DOE), Office of Basic Energy Sciences, Division of Materials Sciences and Engineering, under contract no. DE-AC02-76SF00515 (B.G., M.T., S.T., G.A.D.L.P., H.I.K. and A.M.L.). Use of the Linac Coherent Light Source (LCLS), SLAC National Accelerator Laboratory, is supported by the US Department of Energy, Office of Science, Office of Basic Energy Sciences under contract no. DE-AC02-76SF00515. M.D.S. is supported by a graduate fellowship from the Center for Molecular Analysis and Design (CMAD) at Stanford University. T.W. and F.D. acknowledge funding from an EPSRC NI grant (EP/R044481/1). S.F. acknowledges funding from the EPSRC and the Studienstiftung des deutschen Volkes. T.J.W.V.D.G. acknowledges support from the EPSRC Cambridge NanoDTC, EP/L015978/1 and the Schiff Foundation. S.A.B. acknowledges support from the EPSRC Centre for Doctoral Training in Graphene Technology (EP/L016087/1). F.D. acknowledges support from the DFG Emmy Noether Programme (project no. 387651688) and the Winton Programme for the Physics of Sustainability. T.W. received funding from the European Union's Horizon 2020 research and innovation programme under Marie Skłodowska-Curie grant agreement no. 838772. M.F.T. and H.-G.S. acknowledge support from the Center for Hybrid Organic Inorganic Semiconductors for Energy (CHOISE), an Energy Frontier Research Center funded by the Office of Basic Energy Sciences, Office of Science within the US Department of Energy through contract no. DE-AC36-08G028308 for assistance with the LCLS experiments and interpretation. We thank Y. Rakita for support with single crystal growth.

Author contributions

A.M.L., B.G. and M.D.S. conceived the experiment; B.G. led the LCLS experimental team consisting of B.G., T.J.W.V.D.G., M.D.S., M.T., S.T., H.-G.S., G.A.D.L.P., R.A.-M., T.S. and A.M.L. Data analysis of the time-resolved X-ray scattering measurements was performed by B.G. with contributions from T.J.W.V.D.G., M.T. and S.T. The data were interpreted by B.G. and A.M.L. with contributions from T.J.W.V.D.G., H.-G.S., M.T., S.T., M.F.T. and F.D. Perovskite single crystal samples were synthesized by M.D.S. who also performed their static characterizations. A.M.L. performed the polaron model calculations. T.W., S.A.B., S.F. and F.D. performed the transient reflectivity measurements. S.F. performed the transient grating photoluminescence measurements and static optical characterization. T.W. and F.D. analysed and interpreted the transient reflectivity data. A.M.L., F.D., M.F.T., H.I.K. and D.Z. supervised the research. B.G., A.M.L., T.W. and F.D. wrote the paper with contributions from all authors.

Competing interests

The authors declare no competing interests.

Additional information

Supplementary information is available for this paper at https://doi.org/10.1038/s41563-020-00865-5.

Correspondence and requests for materials should be addressed to A.M.L.

Peer review information *Nature Materials* thanks Paul Beaud, Elbert Chia and Sergei Tretiak for their contribution to the peer review of this work.

Reprints and permissions information is available at www.nature.com/reprints.